

Parallel encoding of recent visual experience and self-motion during navigation in *Drosophila*

Hiroshi M Shiozaki¹ & Hokto Kazama^{1,2}

Animal navigation requires multiple types of information for decisions on directional heading. We identified neural processing channels that encode multiple cues during navigational decision-making in *Drosophila melanogaster*. In a flight simulator, we found that flies made directional choices on the basis of the location of a recently presented landmark. This experience-guided navigation was impaired by silencing neurons in the bulb (BU), a region in the central brain. Two-photon calcium imaging during flight revealed that the dorsal part of the BU encodes the location of a recent landmark, whereas the ventral part of the BU tracks self-motion reflecting turns. Photolabeling-based circuit tracing indicated that these functional compartments of the BU constitute adjacent, yet distinct, anatomical pathways that both enter the navigation center. Thus, the fly's navigation system organizes multiple types of information in parallel channels, which may compactly transmit signals without interference for decision-making during flight.

Animals, including insects, navigate the environment using external and internal cues. For example, visual landmarks are a prominent external cue for spatial orientation^{1,2}. Memories of landmarks are an internal cue by which animals assess the familiarity of visual scenes or orient toward a remembered location^{1,3,4}. Self-motion is another internal cue that is used to keep track of the animal's current spatial position through path integration^{5,6}. Animal navigation therefore requires the integration of multiple types of cues; however, where these cues converge in the nervous system is largely unknown.

In *Drosophila*, ring neurons in the central brain encode the location of visual landmarks^{7,8} and are necessary for spatial orientation requiring visuospatial memory^{4,9–13}. Ring neurons have their dendrites in the BU and their axons in the ellipsoid body (EB) of the central complex (CX)^{7,14–16}, the insect navigation center¹². Another type of neurons have their dendrites in the EB and represent a fly's heading direction on the basis of the information about visual landmark and their own motion^{17–20}. Although these observations suggest the existence of neural codes for visuospatial memory and self-motion upstream of the CX, this has not been identified because recording neural activity in behaving flies^{21,22}, especially those that involve memory, is technically challenging.

We searched for neural circuits encoding navigational cues by developing an experience-guided spatial orientation task that is compatible with neural recording. We found that flies used information about the location of a recently presented landmark to decide heading direction in a flight simulator. This experience-guided flight orientation was impaired by inactivation of ring neurons, suggesting a contribution of the BU. Two-photon calcium imaging in flies performing the task revealed distinct encoding of navigational cues in two populations of neurons in the BU. One population, located in a dorsal part of the BU, responded to a landmark presented in the ipsilateral visual field. Notably, this population was reactivated after

the disappearance of the landmark, indicating a neural code for recent visual experience. Another population, located in a ventral part of the BU, encoded both the fly's turning behavior and landmark location. Furthermore, we found that neurons innervating dorsal and ventral parts of the BU form parallel pathways that reach the CX. These findings indicate that the fly's navigation system has a markedly compact architecture in which a single brain region channels multiple types of information, which may be integrated in the CX circuits to select appropriate flight course.

RESULTS

Recent visual experience guides flight orientation

We first devised a binary choice task for head-fixed flies in a flight simulator (Fig. 1a). The simulator operates in two modes: in a closed-loop mode, in which visual patterns surrounding a fly rotate according to the fly's intended turns in the horizontal plane, and in an open-loop mode, in which patterns remain stationary irrespective of the turns (Fig. 1b,c). Because of the fly's innate tendency to orient toward a dark, vertical bar²³, animals spontaneously chose one of the two bars presented simultaneously in the left and the right visual fields (Supplementary Fig. 1a–c). We then asked whether and how this choice is influenced by a preceding visual stimulus. Specifically, in each trial, a bar (cue stimulus) was transiently presented in either the left or the right visual field. The cue was presented in the open-loop mode so that its location was identical across repeated trials. Following a delay period with no visual patterns, two bars (choice targets) appeared in the closed-loop mode as targets (Fig. 1d). We found that choices were strongly biased toward the uncued side (left choice: $28.0 \pm 3.1\%$ for left cue, $71.9 \pm 3.2\%$ for right cue, $N = 20$ flies, $P < 0.001/2$ for both cues, one-sample t test with Bonferroni correction, the denominator represents the number of comparisons; Fig. 1e,f and Supplementary Video 1). In most trials, flies

¹RIKEN Brain Science Institute, Saitama, Japan. ²Graduate School of Arts and Sciences, The University of Tokyo, Tokyo, Japan. Correspondence should be addressed to H.M.S. (shiozaki.h@gmail.com) or H.K. (hokto_kazama@brain.riken.jp).

Received 22 January; accepted 26 July; published online 4 September 2017; doi:10.1038/nn.4628

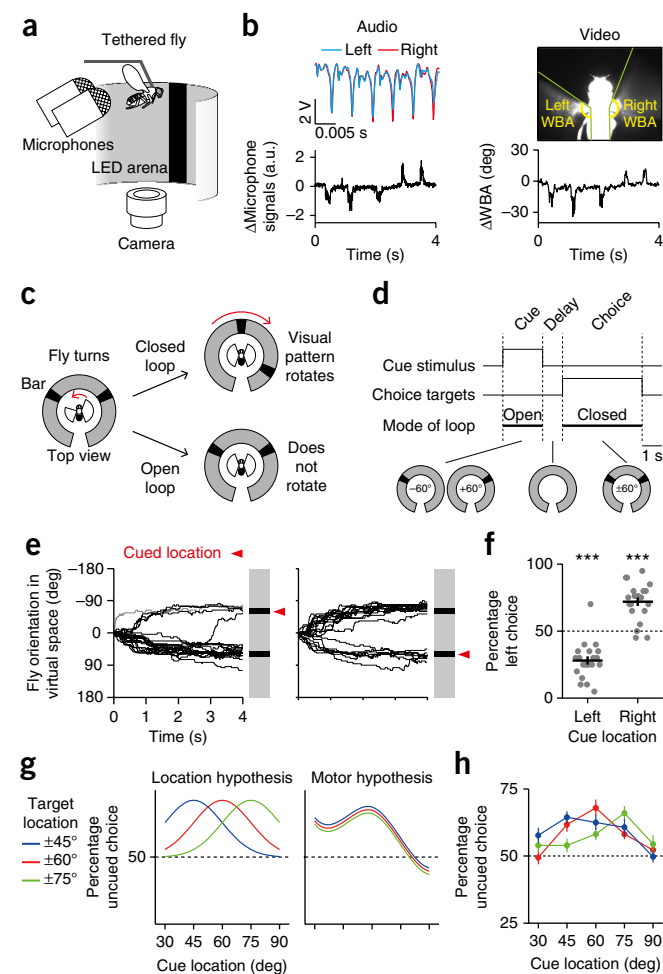


Figure 1 Information about the location of a recent cue guides flight orientation. **(a)** Setup for behavioral experiments. **(b)** Estimation of fly's intended turns in the horizontal plane. Top left, raw microphone signals capturing six wingbeats. Bottom left, the difference between the left and the right microphone signals, the audio-based estimate of turns, was used to drive pattern rotation in the closed-loop mode. Top right, a bottom view of the fly from which the wingbeat angle (WBA) of each wing was estimated. The image is flipped horizontally so that the left wing is displayed on the left side. Bottom right, the difference between the left and the right WBA (Δ WBA), the video-based estimate of turns, was used for offline analyses. **(c)** Two modes of visual pattern presentation. **(d–f)** Cueing experiment. **(d)** Task and stimuli. **(e)** Trajectories of an example fly during the choice period. Each line depicts the trajectory in each trial. We discarded 1 of the 41 trials (gray line in the left panel) from further analyses because of its short reaction time (see Online Methods for the criteria for trial disposal). **(f)** Population summary ($N = 20$ flies). Each dot represents the percentage of left choice trials for a fly, calculated from 20 trials in each cue location. Cueing biased the choice toward the uncued side ($***P < 0.001/2$, one-sample t test with Bonferroni correction, the denominator represents the number of comparisons). Black lines, mean \pm s.e.m. across flies. **(g,h)** Cue/target location experiment. Same task as in the cueing experiment **(d)**, but the location of a cue and targets was varied. **(g)** Predictions of two hypotheses. The ordinate represents the percentage of trials in which the fly chose to orient toward the side where the cue had not been presented. The prediction of the motor hypothesis was generated based on the result of the bar location experiment shown in **Supplementary Figure 1s–u** under the assumption that a stronger intended turn produces a stronger effect (Online Methods). **(h)** Choice bias for each combination of cue and target locations (mean \pm s.e.m. across flies; $N = 20$ flies for each combination). Exact P values for all statistical tests can be found in **Supplementary Table 1**.

turned to the bar at the uncued location soon after (<1 s) its onset and maintained fixation during the rest of the choice period (**Fig. 1e** and **Supplementary Fig. 1d**). Choices were made at random without cueing (left choice: $47.8 \pm 4.1\%$, $N = 20$ flies, $P = 0.60$, one-sample t test), and the magnitude of cue-induced choice bias was comparable to that of innate orientation bias toward a single bar (**Supplementary Fig. 1a–c**). We further found that a shorter cue presentation was sufficient to induce the bias (**Supplementary Fig. 1f,g**), that this bias remained even after a delay of several seconds (**Supplementary Fig. 1h,i**) and that the cueing did not make flies avoid the bar presented at the cued location, but rather reduced its attractiveness (**Supplementary Fig. 1j–l**). The choice bias was still observed when the cue was presented in closed-loop (**Supplementary Fig. 1m,n**), indicating that unsuccessful turns to the cue, as a result of open loop, were not the cause of the choice bias. Finally, similarly to dark bars, bright bars induced orientation toward the uncued side (**Supplementary Fig. 1o,p**) even though the bright bars themselves were not attractive (**Supplementary Fig. 1q,r**). This suggests that adaptation to a bar presented during the cue period alone cannot explain the choice bias that we observed in our assay.

This biased orientation could be explained by at least two hypotheses. One hypothesis, which we term the location hypothesis, assumes that the cueing generates a location-specific effect and that this biases the choice toward the bar at the uncued location. This is reminiscent of novelty preference behavior, a tendency observed in many species to preferentially look at novel objects over familiar ones^{3,13,24,25}. The other hypothesis, the motor hypothesis, assumes that the bias is caused by the history of how much they have turned before the choice. Because flies attempted to turn toward the cue during its presentation (**Supplementary Fig. 1d,e**), this hypothesis explains the bias as an alternating orientation, which has been observed in navigating rodents and insects^{3,26}. To distinguish between the two hypotheses, we varied the locations of a cue and targets. The location hypothesis predicts that the bias would be strongest when the location of a cue and target matches (**Fig. 1g**), whereas the motor hypothesis predicts the strongest bias for the cue location that induces turns most consistently ($\pm 60^\circ$; **Supplementary Fig. 1s–u**), irrespective of target location (**Fig. 1g**). We found that the pattern of choice bias was more consistent with the location hypothesis than the motor hypothesis (**Fig. 1h** and **Supplementary Fig. 1v**; see partial correlation analysis in Online Methods for quantitative assessment). Taken together, our results demonstrate that flies make navigational decisions by using information about the location of a recent landmark.

The BU is involved in experience-guided flight orientation

We hypothesized that ring neurons connecting the BU and the EB might be involved in this experience-guided orientation task because they encode the location of visual landmarks and are required for orientation on the basis of visuospatial memory^{4,9–13}. To test this, we genetically inactivated ring neurons by overexpressing a type of potassium channel (**Fig. 2a**). We used three driver lines that specifically target different subsets of ring neurons (**Fig. 2b** and **Supplementary Fig. 2a**). During the cueing task (**Fig. 1d**), flies with inactivated ring neurons oriented less to the uncued side than control flies (**Fig. 2c**), suggesting that ring neurons causally contribute to experience-guided flight orientation. Although choice biases can be weakened if the inactivation causes flies to choose one side excessively, this was not the case, as when the two bars were presented without cueing, the proportion of choosing one side was similar between flies with and without inactivation (**Supplementary Fig. 2b**). This is in contrast with

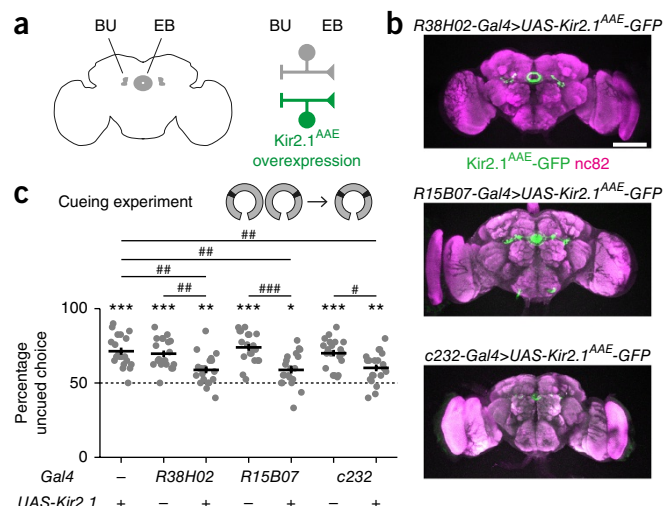


Figure 2 The BU is involved in experience-guided flight orientation. (a) Schematics of the fly brain (left) and ring neurons (right), which have dendrites in the BU and axons in the EB. A type of potassium channel was overexpressed in subsets of ring neurons. (b) Expression patterns of the potassium channel Kir2.1^{AAE} in the brains of three driver lines that target different subsets of ring neurons (R4 neurons by *R38H02-Gal4* (ref. 11), R1 and R4 neurons by *R15B07-Gal4* (ref. 11), and R3 and R4d neurons by *c232-Gal4* (ref. 34)). Brains were immunostained with nc82 (magenta) and an antibody to GFP (green). Scale bar represents 100 μ m. (c) Summary of the choice bias in the cueing experiment ($N = 20$ flies for each genotype). The task was the same as that described in **Figure 1d**. Each dot represents the percentage of trials in which each fly chose to orient toward the uncued side. Black lines, mean \pm s.e.m. across flies. * $P < 0.05/7$, ** $P < 0.01/7$, *** $P < 0.001/7$, one-sample t test with Bonferroni correction. # $P < 0.05/3$, ## $P < 0.01/3$, ### $P < 0.001/3$, two-sample t -test with Bonferroni correction, the denominator represents the number of comparisons. Exact P values for all statistical tests can be found in **Supplementary Table 1**.

columnar neurons in the CX whose inactivation increases turn biases in walking flies²⁷. Orientation toward a dark bar was not impaired by the inactivation of ring neurons except for one driver line in which the mutant flies showed weaker orientation than one of the two control lines (**Supplementary Fig. 2c**). Together, these results suggest that the BU is relevant for the experience-guided flight orientation described in this study.

Two populations of microglomeruli in the BU show distinct task-related activity during experience-guided navigation

We next examined whether and how navigational cues are represented in the BU during the task. The BU is composed of structures called microglomeruli, in which the dendrites of ring neurons and the axons of neurons in the anterior optic tubercle (AOTU) meet (**Fig. 3a**)^{7,8,12,14,15,28–30}. Microglomeruli are considered to be the unit of output from the BU because each ring neuron extends its dendrites to only one microglomerulus^{7,8,14,15}. The BU is highly stereotyped across individuals in terms of the number (66.3 ± 2.5 , mean \pm s.d., $N = 8$ hemispheres in 4 flies, **Fig. 3b**) and arrangement of microglomeruli (**Supplementary Fig. 3a**). To sample from the entire population of microglomeruli in an unbiased way, we pan-neuronally expressed the genetically encoded calcium indicator GCaMP6f and recorded calcium signals from the BU using two-photon microscopy^{7,31} while flies performed the task (**Fig. 3c,d**). We targeted a specific part of the BU in each fly and collectively covered the entire BU by aggregating data across flies (**Fig. 3e,f** and **Supplementary Fig. 3b,c**). During

calcium imaging, flies showed a moderate, but significant, choice bias (uncued choice, $55.4 \pm 1.2\%$, mean \pm s.e.m., $N = 40$ flies, $P < 0.001$, one-sample t test).

We found that microglomeruli showed task-related activity. One representative microglomerulus was activated while the cue was being presented in the ipsilateral, but not contralateral, visual field (**Fig. 3g,h**). Notably, this activation was often followed by transient reactivation in the delay period, during which the cue was no longer present (**Fig. 3g,h** and **Supplementary Video 2**). The timing of reactivation varied from trial to trial (**Fig. 3g,h**), resulting in trial-averaged activity that was consistently higher after ipsilateral than contralateral cue presentation (**Fig. 3h**). The microglomerulus was activated again during the choice period, during which visual stimuli were presented in both visual fields (**Fig. 3g,h**). Another representative microglomerulus showed decreased and increased activity during ipsilateral and contralateral cue presentation, respectively (**Fig. 3i,j**). We found that the activity of this microglomerulus faithfully tracked the dynamics of intended turns, with higher activity for turns toward the contralateral side (**Fig. 3i,j** and **Supplementary Video 3**).

To examine whether this prominent activity during cue presentation is indeed the signature of the BU, we quantified the difference in the activity of each microglomerulus between ipsilateral and contralateral cue presentations, using an index we defined as trial-type preference (Online Methods). This index reflects the selectivity for cue location and/or turns, as these two factors were correlated (for example, flies tended to turn toward the cue during its presentation; **Fig. 3g–j** and **Supplementary Fig. 1d,e**). A substantial proportion of microglomeruli showed higher activity in either ipsilateral (19%, ipsi-prefering population, trial-type preference significantly smaller than 0, $P < 0.05$, permutation test) or contralateral cue presentation (17%, contra-prefering population, trial-type preference significantly larger than 0, $P < 0.05$, permutation test), and the remaining population did not show significant trial-type preference during the cue period (64%, no-preference population, $P > 0.05$, permutation test) (**Fig. 3k–m** and **Supplementary Fig. 4**). Thus, the BU contains two populations of microglomeruli that modulate activity in opposite directions during cue presentation. The preferred cue location, however, was not the only difference in the two populations. Although the ipsi-prefering population was only weakly suppressed by contralateral cue presentation (**Fig. 3l** and **Supplementary Fig. 4a,e**), the contra-prefering population showed strong suppression to ipsilateral cue presentation (**Fig. 3m** and **Supplementary Fig. 4c,e**). Furthermore, the activity of these two populations also differed during the delay period, during which only the ipsi-prefering population showed higher activity after the presentation of ipsilateral than contralateral cues (**Fig. 3l–o** and **Supplementary Fig. 4a,c**). Thus, the two populations of microglomeruli in the BU show qualitatively different task-related activity.

Two populations of microglomeruli differentially encode recent visual experience and self-motion

We next asked whether cue location and self-motion have distinct effects on the activity of the ipsi-prefering and contra-prefering populations, as in the example microglomeruli. To isolate the component of the activity related to intended turns from that related to cue location, we performed a set of linear regression between calcium signals and turns separately for each cue location (**Fig. 4a,b** and **Supplementary Fig. 5**; see Online Methods for details). This regression involved two parameters, the Y-intercept and the slope. During the cue and the delay periods, the Y-intercept represents responses to cue and the slope represents the selectivity for turns. During the



Figure 3 Two populations of microglomeruli in the BU show distinct task-related activity. **(a)** Target brain region, the BU. Left, schematic of the fly brain. Middle, a confocal image showing microglomeruli in the BU. The brain was immunostained with an antibody to GFP that was expressed pan-neuronally. The white outline indicates the boundary of the BU. Scale bar represents 10 μ m. Right, schematic of neurons that compose BU microglomeruli. D, dorsal; V, ventral; L, lateral; M, medial. **(b)** Number of microglomeruli in the BU ($N = 8$ hemispheres in 4 flies). **(c)** Setup for calcium-imaging experiments. **(d)** Task and stimuli. The task was identical to the one in **Figure 1d** except that the delay period was extended to 4 s for better separation of the activity during the cue and the delay periods. **(e)** BU microglomeruli of an example fly expressing GCaMP6f pan-neuronally. Left, all the microglomeruli recorded in this fly ($N = 15$). Middle and right, images of two example microglomeruli, generated by averaging frames of highest intensity (top 5%) for each microglomerulus. Scale bar represents 10 μ m. A, anterior; P, posterior. **(f)** Schematic of the imaged volume in each experiment. **(g,h)** Responses of an example microglomerulus. **(g)** Calcium responses of a microglomerulus (red) and fly's intended turns (black) in three example trials. The cue was presented in the ipsilateral visual field (Ipsi) in the top two trials and the contralateral visual field (Contra) in the bottom trial. Positive and negative Δ WBA represent the intended turn toward the contralateral and the ipsilateral side, respectively. **(h)** Top, responses of the microglomerulus in **g** in each trial ($N = 10$ trials for each cue location). Middle, simultaneously recorded intended turns of the fly. Bottom, the average activity (mean \pm s.e.m. across trials) for each cue location (Ipsi and Contra). Markers on the left of the color plots indicate the trials shown in **g**. **(i,j)** Responses of another example microglomerulus ($N = 12$ trials for each cue location). **(k)** Histogram of the trial-type preference ($N = 566$ microglomeruli in 40 flies), an index quantifying how much the activity of individual microglomeruli differed between ipsilateral and contralateral cue presentations. Blue and vermilion bars represent significant trial-type preference with a higher activity in Ipsi ($N = 107$ microglomeruli in 21 flies) and Contra ($N = 98$ microglomeruli in 17 flies) trials, respectively ($P < 0.05$, permutation test). White bars represent microglomeruli that did not show significant trial-type preference ($P > 0.05$, permutation test; $N = 361$ microglomeruli in 40 flies). **(l,m)** Population-averaged activity for each cue location (mean \pm s.e.m. across microglomeruli) for the ipsi-prefering population (**l**) and the contra-prefering population (**m**). The trial-averaged calcium responses of each microglomerulus were averaged across microglomeruli. **(n)** Distribution of mean Δ F/F of each microglomerulus during the last 3 s of the delay period, plotted separately for each cue location and population. Box plots indicate median, quartiles and range. $**P < 0.01/2$, $***P < 0.001/2$, one-sample t test with Bonferroni correction, the denominator represents the number of comparisons. $###P < 0.001$, paired t test. **(o)** Distribution of the difference in mean Δ F/F between cue locations during the last 3 s of the delay period. $***P < 0.001$, one-way ANOVA followed by *post hoc* Tukey's HSD test. Data are presented as in **n**. Exact P values for all statistical tests can be found in **Supplementary Table 1**.

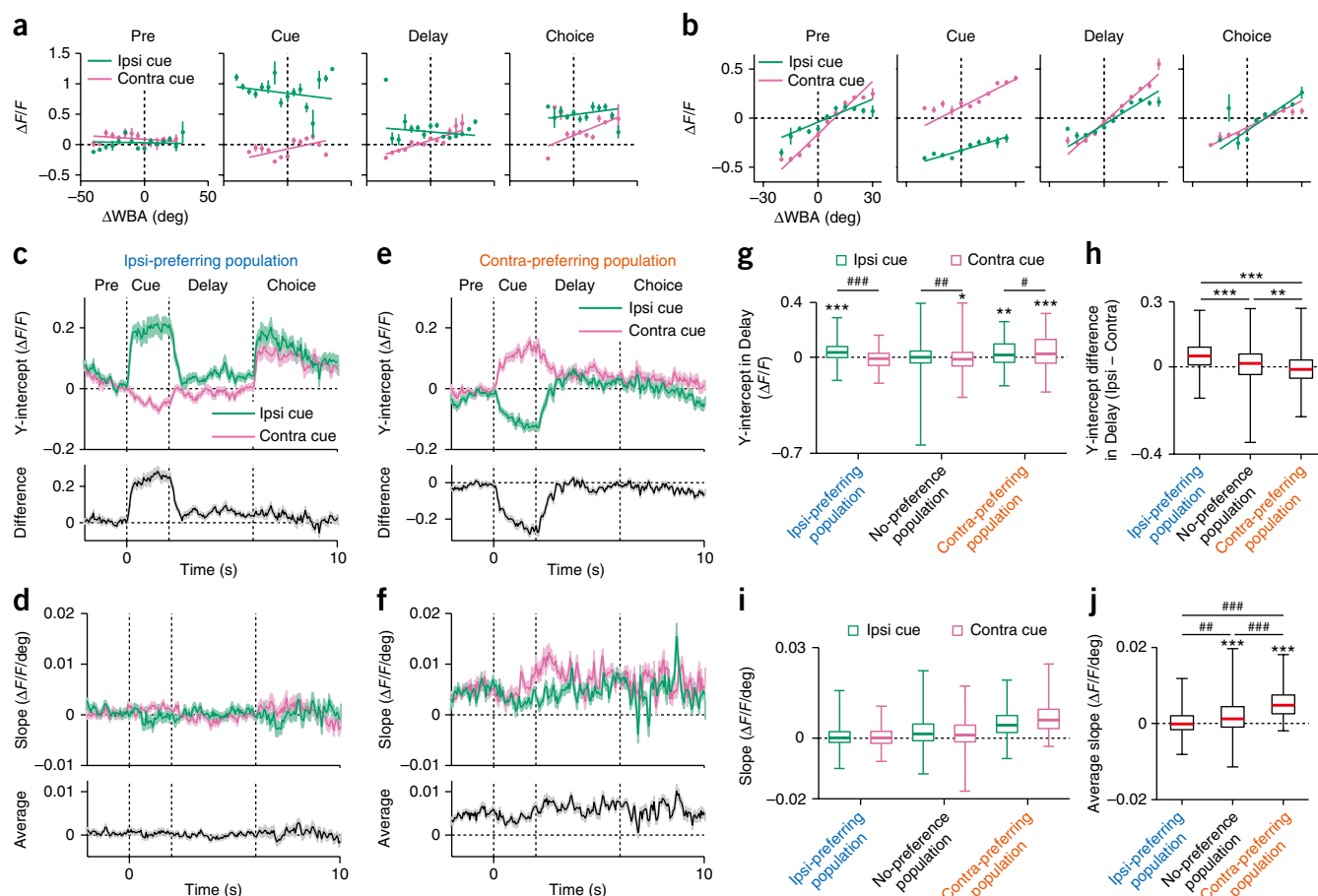


Figure 4 Two populations of microglomeruli selectively encode recent visual experience and self-motion, respectively. (a) Separation of cue-location-related and intended-turn-related components of the activity for the example microglomerulus shown in **Figure 3g,h**. Dots and error bars represent calcium responses (mean \pm s.e.m. across time frames) calculated for every 5 degrees of ΔWBA . Data were aggregated across trials ($N = 10$ trials for each cue location). Lines indicate regression fit. The slopes of the regression lines represent the responses related to intended turns, whereas the Y-intercepts describe the responses not explained by turns (for example, visual responses). (b) Data are presented as in **a**, but for the other example shown in **Figure 3i,j**. (c–f) Time course of regression parameters (mean \pm s.e.m. across microglomeruli) for the ipsi-prefering population (c,d) ($N = 107$ microglomeruli in 21 flies) and the contra-prefering population (e,f) ($N = 98$ microglomeruli in 17 flies). (c,e) Y-intercept. (d,f) Slope. (g) Distribution of the average Y-intercept of each microglomerulus during the last 3 s of the delay period, plotted separately for each cue location and population. Box plots indicate median, quartiles and range. * $P < 0.05/2$, ** $P < 0.01/2$, *** $P < 0.001/2$, one-sample t -test with Bonferroni correction, the denominator represents the number of comparisons. # $P < 0.05$, ## $P < 0.01$, ### $P < 0.001$, paired t -test. (h) Distribution of the difference in the average Y-intercepts between cue locations during the last 3 s of the delay period. Box plots indicate median, quartiles and range. ** $P < 0.01$, *** $P < 0.001$, one-way ANOVA followed by *post hoc* Tukey's HSD test. (i) Data are presented as in **g**, but for the average slope during the entire task period. (j) Data are presented as in **h**, but for the slope averaged across time, trials and cue locations. *** $P < 0.001$, one-sample t -test. ## $P < 0.01$, ### $P < 0.001$, one-way ANOVA followed by *post hoc* Tukey's HSD test. Exact P values for all statistical tests can be found in **Supplementary Table 1**.

choice period, the Y-intercept and the slope also represent responses to choice targets and the motion of the targets, respectively.

This analysis revealed distinct encoding of navigational cues by the two populations. The ipsi-prefering population encoded cue location during and after its presentation. The Y-intercept increased in ipsilateral cue trials during the cue period and persisted throughout the delay (**Fig. 4c,g,h** and **Supplementary Fig. 6a,i,j**). The slope was close to zero throughout the trial (**Fig. 4d,i,j** and **Supplementary Fig. 6b**). By contrast, the contra-prefering population encoded cue location only during its presentation, and self-motion during all of the periods. The Y-intercept showed symmetric changes during the cue period, with an increase for contralateral cue, and differed only weakly during the delay period (**Fig. 4e,g,h** and **Supplementary Fig. 6e,i,j**). The slope was heightened throughout the trial, indicating an invariant selectivity for turns (**Fig. 4f,i,j**

and **Supplementary Fig. 6f**). Consistent with this, the activity of this population was correlated with turns even after removing the cue location component (correlation coefficient, 0.22 ± 0.02 , mean \pm s.e.m., $N = 98$ microglomeruli; **Supplementary Fig. 7c**). This correlation was likely to be determined by the difference in the left and the right wingbeat angles, a proxy for yaw torque^{32,33}, and by slow changes in turning behavior (**Supplementary Fig. 7**). The slope scaled with the difference in Y-intercept across microglomeruli (**Supplementary Fig. 6k**), indicating that cue location and self-motion signals are not carried by separate microglomeruli, but instead by the same set of microglomeruli. The no-preference population showed small changes in the Y-intercept and the slope (**Fig. 4g–j** and **Supplementary Fig. 6c,d,g–j**). These results indicate that the two neural populations in the BU are functionally distinct: encoding cue location, its history and self-motion differentially.

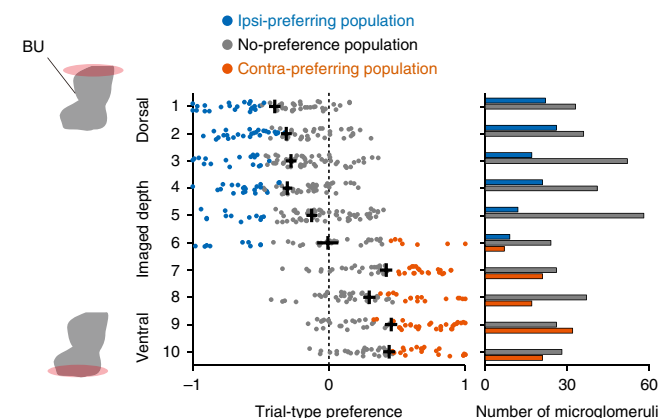


Figure 5 Two populations of microglomeruli are spatially segregated. Left, relationship between imaged depth and the trial-type preference during the cue period. Each dot represents a microglomerulus. Black lines represent mean \pm s.e.m. across microglomeruli. Right, the number of recorded microglomeruli in each population plotted against the imaged depth (blue, ipsi-preferring population; gray, no-preference population; vermillion, contra-preferring population).

Two populations of microglomeruli are spatially segregated

Notably, we found that distinct encoding of navigational cues tightly parallels the anatomical organization of the BU: the ipsi-preferring and the contra-preferring populations were located almost exclusively in the dorsal and the ventral halves of the BU (dBU and vBU), respectively (Fig. 5 and Supplementary Fig. 8a,b). On a finer scale, the ipsi-preferring population was preferentially found in the lateral and medial parts of the dBU, whereas the contra-preferring population was localized to the anterior-lateral part of the vBU (Supplementary Fig. 8). Thus, complementary parts of the BU encode distinct navigational cues during tethered flight.

Microglomeruli encoding landmark location also encode its history as transient activity

Considering that different microglomeruli in the dBU have their visual receptive fields at different locations^{7,8,15}, we hypothesized that the location of a recent landmark is encoded in microglomeruli with receptive fields at the cue location. Indeed, we found that dBU microglomeruli that responded more strongly to the cue showed stronger delay-period activity (Supplementary Fig. 9). Notably, the delay-period activity in the ipsi-preferring population was sufficiently reliable to explain the magnitude of choice bias of the flies (Supplementary Fig. 9c).

Inspection of individual trials revealed transient increases in calcium signals during the delay period (Fig. 3g and Supplementary Fig. 10a–c). We found that these transients occurred more frequently after the ipsilateral than the contralateral cue presentation, especially in the ipsi-preferring population (Supplementary Fig. 10d,e). The magnitude and temporal dynamics of transients were largely invariant to cue locations and the type of populations (Supplementary Fig. 10f–s). Stronger responses to the cue tended to be followed by a larger number of transients in ipsilateral, but not contralateral, cue trials (Supplementary Fig. 11a,b,e,f). Responses in the delay period increased with the number of transients per trial (Supplementary Fig. 11a,c–e,g,h), suggesting that more frequent occurrence of transients underlies the larger delay-period activity in ipsilateral cue trials. However, persistent components might also contribute because the activity was higher in ipsilateral than in contralateral cue trials

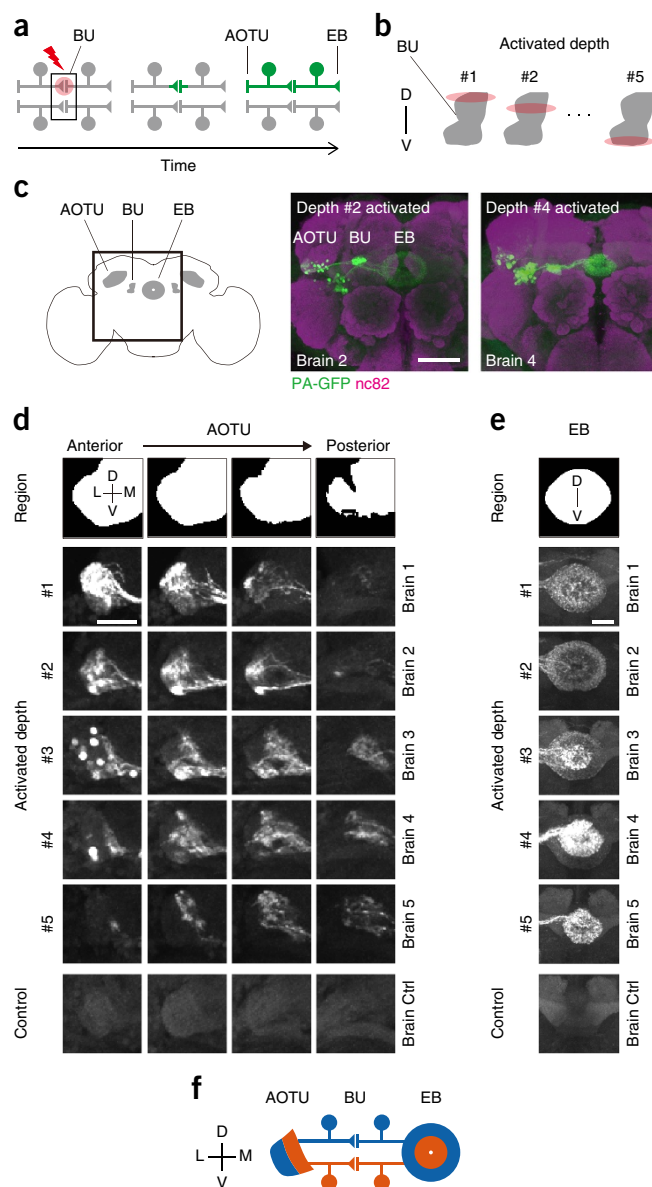


Figure 6 Dorsal and ventral parts of the BU constitute parallel pathways. (a) Selective visualization of subpopulations of BU neurons with PA-GFP. Following application of a pulsed laser to a volume of the BU (red), PA-GFP undergoes photoconversion (green) and diffuses to the entire structure of neurons that innervate the target volume. (b) Schematic of the photoactivated volume in each brain. (c) Left, schematic indicating the imaged region of the brain. Right, projections of confocal stacks of two representative brains in which the dorsal and the ventral parts of the BU were photoactivated, respectively. Brains were immunostained with nc82 (magenta). Green, PA-GFP. Scale bar represents 50 μ m. (d) Photolabeling in the AOTU. A volume that covers the lateral and the intermediate zones of the AOTU was divided along the anterior-posterior axis. Four images aligned in a row are projections of confocal stacks for each subvolume (six frames, 3.72 μ m) obtained from one brain. Cell bodies are visible in some images (for example, the leftmost panel of brain #3). Top, the region of the AOTU in a standard brain (Online Methods). Bottom, images of a control brain in which no photoactivation was applied. Scale bar represents 20 μ m. (e) Photolabeling in the EB. The same brains are shown as in d. Each image, obtained from one brain, is a projection of a confocal stack covering the EB. Top, the region of the EB in a standard brain. Bottom, an image of the control brain. Scale bar represents 20 μ m. (f) Schematic of the connections between the AOTU, the BU and the EB revealed by the photolabeling experiment.

even when an equal number of transients occurred in both trials (Supplementary Fig. 11a,c–e,g,h). These results suggest that the location of the previous cue is encoded by transient reactivation of the dBU microglomeruli that have responded to the cue.

Two populations of microglomeruli constitute parallel pathways

The spatial segregation of functionally distinct microglomeruli between the dBU and the vBU suggests that there are differences in the underlying neuronal networks. To test this, we pan-neuronally expressed photoactivatable GFP (PA-GFP) and visualized the morphology of neurons innervating specific parts of the BU (Fig. 6a,b and Supplementary Fig. 12a). Consistent with previous reports^{8,14,15,28–30}, photoactivation strongly labeled two brain regions outside of the BU: the AOTU (an input region) and the EB (an output region) (Fig. 6c and Supplementary Fig. 12b,c). Notably, the distribution of photolabeling signals in the AOTU and the EB differed depending on the depth of the photoactivated BU. Photoactivation of the dBU labeled anterolateral regions of the AOTU and outer layers of the EB, whereas photoactivation of the vBU labeled complementary regions in both the AOTU and the EB (Fig. 6d,e and Supplementary Fig. 13a,b), consistent with the findings of a recent study¹⁵. This result agrees with the reports that different types of ring neurons, defined by the location of axons, have dendrites in different parts of the BU (Supplementary Fig. 14)^{7,15,34}. A separate experiment revealed the existence of finer structures in the vBU (Supplementary Fig. 13c–f), consistent with the localization of the contra-preferring microglomeruli (Supplementary Fig. 8c). Together with the functional analysis, our data suggest that recent visual experience and self-motion signals are selectively transmitted through parallel neural pathways from the AOTU to the BU, and then to the EB (Fig. 6f).

DISCUSSION

We identified the neural circuits encoding navigational cues in the *Drosophila* brain by developing an experience-guided choice task in a virtual environment. We focused on an innate behavior, preferential orientation toward novel objects, and found that flies retain the information about the location of a visual landmark for several seconds and oriented toward a landmark presented at a novel location (Fig. 1 and Supplementary Fig. 1). Our findings complement previous reports on the preference for novel shapes^{13,25} and suggest that novelty preference encompasses multiple properties of objects in flies as with mammals^{3,24}.

Although recent visual experience led to novelty preference behavior in our task, similar types of experiences can elicit different behaviors^{4,35–37}. For example, a study has shown that freely walking flies orient toward the location of a recently presented landmark⁴. In that study, the fly initially walked toward a landmark, which suddenly disappeared and another landmark appeared laterally to the fly. This second landmark also disappeared after the fly turned toward it. Afterwards, the fly tended to orient toward the location at which the first landmark was presented. This orientation is purely based on recent experience, as no landmarks were present, whereas flies' choices relied on both recent experience and landmarks in our study. Thus, the information about the location of a recent landmark might drive different behaviors (for example, orientation toward the remembered location and novelty preference) depending on visual environments.

Although a number of behavioral genetic studies in flies, including ours, have demonstrated a causal role of ring neurons in memory-guided orientation^{4,9–13}, the lack of physiological measurements has made it impossible to determine whether these neurons represent

memory or are involved in memory acquisition or retrieval. Our recordings from the BU, where the dendrites of ring neurons reside, provide direct evidence for encoding of the location of a recent landmark in the dBU, which is represented as increased activity of microglomeruli with receptive fields at the landmark location (Figs. 3–5 and Supplementary Figs. 4, 6, 8 and 9). Incidentally, the receptive field size of these microglomeruli^{7,8,15} was similar to the spatial extent of the cueing effect that we behaviorally characterized (Fig. 1h). Thus, the dBU neurons may encode a history of stimulus location by maintaining the representation generated during stimulus presentation, as in some mammalian neurons^{38,39}. A recent study has reported that the activity of ring neurons in quiescent flies depends on the recent history of visual stimuli, which can be described by a biphasic temporal filter⁸. This mechanism is unlikely to explain the representation of recent landmark location that we studied because the biphasic filter predicts that the delay-period activity would be stronger after contralateral than ipsilateral cue presentation and would decay within 3 s, neither of which we observed. Thus, the form of history representation might be dependent on the behavioral state. It remains to be determined whether the history representation in the dBU that we have described has a causal role in the experience-guided orientation.

Recent studies have shown that neurons innervating the EB represent a fly's heading direction based on visual landmarks during tethered walking and flight^{17–20}. This representation was present even in flies walking in the dark^{17,19,20}, suggesting that information about self-motion that is provided to this brain region. We identified this information in the vBU pathway reaching the EB in flying flies (Figs. 3–5 and Supplementary Figs. 5–7). However, the information about self-motion is not sufficient to update the heading direction representation during tethered flight because this representation remained stationary in the dark¹⁸. Thus, self-motion signals in the vBU might be involved in the heading direction representation only in the presence of visual landmarks or, alternatively, drive turning behavior, as stimulation of a subset of CX neurons produces left or right turns in cockroaches⁴⁰. Although the function of these self-motion signals is still unknown, our data indicate that the vBU encodes visual and motor information that is relevant for navigation.

What is the origin of self-motion signals in the vBU? The expression patterns of synaptic proteins indicate that neurons connecting the AOTU and the BU have dendrites in the AOTU and axons in the BU^{8,15}, and ring neurons have dendrites in the BU and axons in the EB^{7,15,16}. These data suggest that self-motion signals in the vBU are transmitted from the AOTU. On the other hand, a recent study proposed that self-motion information can reach ring neurons through axo-axonal interaction⁴¹. Thus, self-motion signals in the vBU might originate from CX neurons that represent heading direction^{17–20}. Another candidate is the connections between the BU and the lateral accessory lobe¹⁴, which contains descending neurons⁴², although our photolabeling experiments suggest that such connections are scarce. Identification of the flow of self-motion signals during navigation is a prerequisite for understanding the computations performed by the BU and the CX networks.

We found that the vBU encodes a slow component of turning behavior in flying flies (Supplementary Fig. 7). In contrast, neurons in the fly visual system encode a fast component of flight turning behavior (body saccades), which is likely to be used to cancel out the visual motion signals induced by self-movement^{43,44}. A descending neuron comprising the motor system also encodes a fast, but not a slow, component of flight turns⁴⁵. Thus, slow and fast components of flight turning behavior may be encoded by different brain regions to support distinct functions.

Although previous studies have shown that different types of ring neurons are necessary for different aspects of memory-guided orientation^{4,9–11,13}, physiological accounts have been scarce. Cell-type-specific roles may stem from differences in the types of signals these ring neurons carry. However, it is also possible that the differential signals arise only after processing in the downstream circuits. Our results indicate that the dBU and the vBU, which are innervated by different types of ring neurons (**Supplementary Fig. 14**), carry distinct signals. The dBU and the vBU encode past visual experience and self-motion, respectively. They also differ in landmark encoding: microglomeruli in the dBU prefer the ipsilateral visual field with unilateral receptive fields, whereas microglomeruli in the vBU prefer the contralateral visual field with bilateral receptive fields (**Fig. 4**)^{7,8,15}. These distinct signals are likely integrated in downstream circuits to generate a representation of heading direction or to guide actions. Anatomical evidence supports the idea that such integration could occur in the EB because dendrites of certain neurons are well positioned to sample inputs from multiple types of ring neurons⁴⁶.

Our recording in behaving flies revealed parallel organization of input channels in the navigation system, which may enable signal transmission without interference for selecting appropriate flight course. This architecture is markedly compact compared with mammalian brains, in which different navigational cues are represented in distributed brain regions^{6,47–49}. Neural recording in task-performing *Drosophila* complements the existing advantages of this model organism, providing a framework for studying how the brain implements the computations underlying navigational decision-making.

METHODS

Methods, including statements of data availability and any associated accession codes and references, are available in the [online version of the paper](#).

Note: Any Supplementary Information and Source Data files are available in the online version of the paper.

ACKNOWLEDGMENTS

We thank Y. Aso, G. Rubin, R. Wilson and G. Davis for gifts of fly stocks, K. Ohta for the backcross of flies, L. Badel for help in developing task control programs, G. Maimon for advice on preparation, RIKEN BSI-Olympus Collaboration Center for imaging equipment and software, members of the Kazama laboratory for their support and comments on the manuscript, and S. Fujisawa, Q. Gaudry, A. Nose, N. Uchida and C. Yokoyama for comments on the manuscript. This work was supported by the RIKEN Special Postdoctoral Researchers Program (H.M.S.), JSPS KAKENHI Grant Numbers JP23680044, JP25115732 (H.K.), JP25750410, JP15K18352 (H.M.S.), and RIKEN Brain Science Institute (H.K.).

AUTHOR CONTRIBUTIONS

H.M.S. collected and analyzed the data. H.M.S. and H.K. designed the study and wrote the manuscript.

COMPETING FINANCIAL INTERESTS

The authors declare no competing financial interests.

Reprints and permissions information is available online at <http://www.nature.com/reprints/index.html>. Publisher's note: Springer Nature remains neutral with regard to jurisdictional claims in published maps and institutional affiliations.

- Collett, T.S. & Collett, M. Memory use in insect visual navigation. *Nat. Rev. Neurosci.* **3**, 542–552 (2002).
- Collett, T.S. & Graham, P. Animal navigation: path integration, visual landmarks and cognitive maps. *Curr. Biol.* **14**, R475–R477 (2004).
- Dudchenko, P.A. An overview of the tasks used to test working memory in rodents. *Neurosci. Biobehav. Rev.* **28**, 699–709 (2004).
- Neuser, K., Triphan, T., Mronz, M., Poeck, B. & Strauss, R. Analysis of a spatial orientation memory in *Drosophila*. *Nature* **453**, 1244–1247 (2008).
- Collett, T.S. & Collett, M. Path integration in insects. *Curr. Opin. Neurobiol.* **10**, 757–762 (2000).

- McNaughton, B.L., Battaglia, F.P., Jensen, O., Moser, E.I. & Moser, M.B. Path integration and the neural basis of the 'cognitive map'. *Nat. Rev. Neurosci.* **7**, 663–678 (2006).
- Seelig, J.D. & Jayaraman, V. Feature detection and orientation tuning in the *Drosophila* central complex. *Nature* **503**, 262–266 (2013).
- Sun, Y. *et al.* Neural signatures of dynamic stimulus selection in *Drosophila*. *Nat. Neurosci.* **20**, 1104–1113 (2017).
- Guo, C. *et al.* A conditioned visual orientation requires the ellipsoid body in *Drosophila*. *Learn. Mem.* **22**, 56–63 (2014).
- Kuntz, S., Poeck, B., Sokolowski, M.B. & Strauss, R. The visual orientation memory of *Drosophila* requires Foraging (PKG) upstream of Ignorant (RSK2) in ring neurons of the central complex. *Learn. Mem.* **19**, 337–340 (2012).
- Ofstad, T.A., Zuker, C.S. & Reiser, M.B. Visual place learning in *Drosophila melanogaster*. *Nature* **474**, 204–207 (2011).
- Pfeiffer, K. & Homberg, U. Organization and functional roles of the central complex in the insect brain. *Annu. Rev. Entomol.* **59**, 165–184 (2014).
- Solanki, N., Wolf, R. & Heisenberg, M. Central complex and mushroom bodies mediate novelty choice behavior in *Drosophila*. *J. Neurogenet.* **29**, 30–37 (2015).
- Hanesch, U., Fischbach, K.F. & Heisenberg, M. Neuronal architecture of the central complex in *Drosophila melanogaster*. *Cell Tissue Res.* **257**, 343–366 (1989).
- Omoto, J.J. *et al.* Visual input to the *Drosophila* central complex by developmentally and functionally distinct neuronal populations. *Curr. Biol.* **27**, 1098–1110 (2017).
- Young, J.M. & Armstrong, J.D. Structure of the adult central complex in *Drosophila*: organization of distinct neuronal subsets. *J. Comp. Neurol.* **518**, 1500–1524 (2010).
- Green, J. *et al.* A neural circuit architecture for angular integration in *Drosophila*. *Nature* **546**, 101–106 (2017).
- Kim, S.S., Rouault, H., Druckmann, S. & Jayaraman, V. Ring attractor dynamics in the *Drosophila* central brain. *Science* **356**, 849–853 (2017).
- Seelig, J.D. & Jayaraman, V. Neural dynamics for landmark orientation and angular path integration. *Nature* **521**, 186–191 (2015).
- Turner-Evans, D. *et al.* Angular velocity integration in a fly heading circuit. *Elife* **6**, e23496 (2017).
- Maimon, G., Straw, A.D. & Dickinson, M.H. Active flight increases the gain of visual motion processing in *Drosophila*. *Nat. Neurosci.* **13**, 393–399 (2010).
- Seelig, J.D. *et al.* Two-photon calcium imaging from head-fixed *Drosophila* during optomotor walking behavior. *Nat. Methods* **7**, 535–540 (2010).
- Gotz, K.G. Course-control, metabolism and wing interference during ultralong tethered flight in *Drosophila melanogaster*. *J. Exp. Biol.* **128**, 35–46 (1987).
- Antunes, M. & Biala, G. The novel object recognition memory: neurobiology, test procedure, and its modifications. *Cogn. Process.* **13**, 93–110 (2012).
- Dill, M. & Heisenberg, M. Visual pattern memory without shape recognition. *Phil. Trans. R. Soc. Lond. B* **349**, 143–152 (1995).
- Kennedy, J.S. Zigzagging and casting as a programmed response to wind-borne odor: a review. *Physiol. Entomol.* **8**, 109–120 (1983).
- Buchanan, S.M., Kain, J.S. & de Bivort, B.L. Neuronal control of locomotor handedness in *Drosophila*. *Proc. Natl. Acad. Sci. USA* **112**, 6700–6705 (2015).
- Ito, M., Masuda, N., Shinomiya, K., Endo, K. & Ito, K. Systematic analysis of neural projections reveals clonal composition of the *Drosophila* brain. *Curr. Biol.* **23**, 644–655 (2013).
- Wong, D.C. *et al.* Postembryonic lineages of the *Drosophila* brain. II. Identification of lineage projection patterns based on MARCM clones. *Dev. Biol.* **384**, 258–289 (2013).
- Yu, H.H. *et al.* Clonal development and organization of the adult *Drosophila* central brain. *Curr. Biol.* **23**, 633–643 (2013).
- Weir, P.T. & Dickinson, M.H. Functional divisions for visual processing in the central brain of flying *Drosophila*. *Proc. Natl. Acad. Sci. USA* **112**, E5523–E5532 (2015).
- Gotz, K.G., Hengstenberg, B. & Biesinger, R. Optomotor control of wing beat and body posture in *Drosophila*. *Biol. Cybern.* **35**, 101–112 (1979).
- Tammero, L.F., Frye, M.A. & Dickinson, M.H. Spatial organization of visuomotor reflexes in *Drosophila*. *J. Exp. Biol.* **207**, 113–122 (2004).
- Renn, S.C. *et al.* Genetic analysis of the *Drosophila* ellipsoid body neuropil: organization and development of the central complex. *J. Neurobiol.* **41**, 189–207 (1999).
- Koenig, S., Wolf, R. & Heisenberg, M. Visual attention in flies: dopamine in the mushroom bodies mediates the after-effect of cueing. *PLoS One* **11**, e0161412 (2016).
- Koenig, S., Wolf, R. & Heisenberg, M. Vision in flies: measuring the attention span. *PLoS One* **11**, e0148208 (2016).
- Sareen, P., Wolf, R. & Heisenberg, M. Attracting the attention of a fly. *Proc. Natl. Acad. Sci. USA* **108**, 7230–7235 (2011).
- Barak, O. & Tsodyks, M. Working models of working memory. *Curr. Opin. Neurobiol.* **25**, 20–24 (2014).
- Wang, X.J. Synaptic reverberation underlying mnemonic persistent activity. *Trends Neurosci.* **24**, 455–463 (2001).
- Martin, J.P., Guo, P., Mu, L., Harley, C.M. & Ritzmann, R.E. Central-complex control of movement in the freely walking cockroach. *Curr. Biol.* **25**, 2795–2803 (2015).

41. Kuntz, S., Poeck, B. & Strauss, R. Visual working memory requires permissive and instructive NO/cGMP signaling at presynapses in the *Drosophila* central brain. *Curr. Biol.* **27**, 613–623 (2017).
42. Turner-Evans, D.B. & Jayaraman, V. The insect central complex. *Curr. Biol.* **26**, R453–R457 (2016).
43. Kim, A.J., Fenk, L.M., Lyu, C. & Maimon, G. Quantitative predictions orchestrate visual signaling in *Drosophila*. *Cell* **168**, 280–294 (2017).
44. Kim, A.J., Fitzgerald, J.K. & Maimon, G. Cellular evidence for efference copy in *Drosophila* visuomotor processing. *Nat. Neurosci.* **18**, 1247–1255 (2015).
45. Schnell, B., Ros, I.G. & Dickinson, M.H. A descending neuron correlated with the rapid steering maneuvers of flying *Drosophila*. *Curr. Biol.* **27**, 1200–1205 (2017).
46. Wolff, T., Iyer, N.A. & Rubin, G.M. Neuroarchitecture and neuroanatomy of the *Drosophila* central complex: a GAL4-based dissection of protocerebral bridge neurons and circuits. *J. Comp. Neurol.* **523**, 997–1037 (2015).
47. Kropff, E., Carmichael, J.E., Moser, M.B. & Moser, E.I. Speed cells in the medial entorhinal cortex. *Nature* **523**, 419–424 (2015).
48. Spellman, T. *et al.* Hippocampal-prefrontal input supports spatial encoding in working memory. *Nature* **522**, 309–314 (2015).
49. Taube, J.S. The head direction signal: origins and sensory-motor integration. *Annu. Rev. Neurosci.* **30**, 181–207 (2007).

ONLINE METHODS

Animals. Flies (*Drosophila melanogaster*) were raised on a standard cornmeal agar under a 12-h/12-h light/dark cycle at 24 °C. All experiments were performed on female flies 2–3 d after eclosion. We conducted behavioral, behavioral genetics and calcium imaging experiments 0–4 h before the light-to-dark transition because flies show enhanced locomotor activity around light-dark transitions under standard laboratory conditions⁵⁰. For experiments exclusively measuring behavior (behavioral experiments), we used a laboratory stock that was established from flies caught in the wild by the Michael Dickinson Laboratory⁵¹. We refer to these animals as wild-type flies. All transgenic flies were the progeny of flies that had been backcrossed to the wild-type strain for six generations, except for the ones used in PA-GFP and immunostaining experiments which involved crossing of flies that were not backcrossed. Genotypes of flies used in each figure are listed in **Supplementary Table 2**.

The wild-type flies were a gift from R. Wilson. *UAS-IVS-Syn21-mC3PA-GFP-p10(attP2)* and *UAS-IVS-Syn21-mC3PA-GFP-p10(VK00005)* (ref. 52) were gifts from Y. Aso and G. Rubin. *UAS-Kir2.1^{AAE}-GFP* (ref. 53) flies were a gift from G. Davis. A pan-neuronal Gal4 driver *R57C10-Gal4(attP2)* (ref. 54), *UAS-IVS-mCD8::GFP(attP40)* (ref. 55), *UAS-IVS-GCaMP6f(attP40)* (ref. 56), *c42-Gal4*, *c232-Gal4* (ref. 57), *R15B07-Gal4(attP2)*, *R28D01-Gal4(attP2)*, *R38H02-Gal4(attP2)*, *R64H04-Gal4(attP2)* (ref. 54), *UAS-IVS-mCD8::RFP(attP18)*, *LexAop2-mCD8::GFP(attP8)*, *R57C10-lexA* (ref. 55) were obtained from the Bloomington *Drosophila* Stock Center.

Fly preparation. The fly was briefly (<1 min) anesthetized on ice and placed in a custom-made holding device fixed to a Peltier plate held at 4 °C. This device kept the fly's body at a specific angle. In calcium imaging experiments, parts of the legs were removed to achieve longer flight as described in ref. 21. The fly was then fixed using UV glue to a custom-made holding plate, carved out of a piece of Delrin plastic. The design of the plate was tailored to each experiment. For behavioral and behavioral genetics experiments, we used a plate that has a pin-like protrusion to which the fly's thorax was attached. For calcium imaging experiments, we used a plate similar to the one designed for whole-cell recordings from head-fixed flying flies²¹. In both types of experiments, the head faced slightly upward (0–10°) and the long axis of the body tilted approximately 30° down from the horizontal plane. To reduce the brain motion, the head and the proboscis were glued to the thorax and the head, respectively. In calcium imaging experiments, a small portion of eyes (<20% of the vertical extent) projected through the hole to the side of the objective lens.

Wingbeat measurement. To estimate the fly's intended turns in the horizontal plane (yaw axis), we recorded a bottom view of the wings using a camera (GE680, Prosilica) with a periscopic lens (InfinitiStix 90°, working distance 94 mm, magnification 1.0 ×, Infinity) as described in ref. 21. Wings were illuminated with 850-nm light (SFH 4236, OSRAM) delivered by a pair of optic fibers (FT1500UMT, Thorlabs), each targeting a respective wing from the front. Movies were acquired at 100 frames per s using open-source software FView (ref. 58). In calcium imaging experiments, we placed a shortpass filter (FES0850, Thorlabs) on the periscopic lens to prevent the detection of the excitation light for GCaMP6f. We also recorded the sound of the wingbeat using a pair of microphones (AT9904, audio-technica) attached to an amplifier (AT-MA2, audio-technica). Each microphone aimed toward either the left or the right wing from behind the fly. Audio signals were recorded at 10 kHz.

Visual stimuli. Flies viewed visual stimuli presented in a cylindrical LED arena⁵⁹ (Mettrix Technology). The arena consisted of 88 × 24 pixels and subtended the visual angle of 330° in azimuth and 58° in elevation. The fly's head was located at the cylinder's longitudinal center and the horizontal plane 5 mm above the top edge of the arena. Consequently, visual stimuli subtended the lower visual field. A small region of the arena in the back (90° × 39°) was occluded by the microphones and thus invisible to flies. Visual patterns were updated at 200 Hz.

The arena was composed of green LEDs (568 nm) in behavioral experiments and blue LEDs (470 nm) in behavioral genetics and calcium imaging experiments. The blue LEDs were covered with four layers of a color filter (Roscolux #39, Rosco) to minimize the bleed-through of light from the arena to the fluorescence detector. For the patterns used in the calcium imaging experiments, the magnitude of bleed-through was 1.3–3.3% of the mean baseline fluorescence of

microglomeruli. The visual stimulus was a dark vertical bar of 4 × 24 pixels (subtending 15° × 58°, 6.0 cd/m² for green LEDs, 0.0 cd/cm² for blue LEDs) presented in a uniform background (25.0 cd/m² in behavioral experiments, 0.02 cd/cm² in behavioral genetics and calcium imaging experiments) except for two behavioral experiments (**Supplementary Fig. 10–r**) where a bright vertical bar of 4 × 24 pixels (50.0 cd/m²) was presented in the uniform background (25.0 cd/m²).

Turn estimation and closed loop flight. We used wingbeat video data for offline analyses of intended turns. In each frame of video data, we calculated the angle of each wing (WBA) based on the method described in ref. 21. We then estimated intended turns by taking the difference between the left and the right WBA (ΔWBA). This measure has been shown to highly correlate with yaw torque^{32,33}.

This video data, however, is not suitable for online estimation of turns because it is high dimensional and requires substantial time for analysis. We therefore used microphone recording of wingbeat, which is low dimensional but provides information quantitatively similar to optical recording of wingbeat⁵¹. For the data from each microphone, the difference between the minimum and the maximum values was calculated every 5 ms. After this value was multiplied by a gain factor separately for each wing (see below), an estimate of turn was obtained as the difference in this value between wings. Turns estimated in this way were substantially correlated with ΔWBA calculated from video data (average Pearson's correlation coefficient across 20 flies used in the cueing experiment (**Fig. 1d,e**), 0.55 ± 0.18, mean ± s.d.).

Every 5 ms, the visual pattern in the arena was rotated if the estimated turn exceeded a threshold, which was fixed across experiments. The pattern was rotated one pixel when the turn was between one and two times the threshold, two pixels when it was between two and three times the threshold, and so on. Thus, the estimated turn defined the angular velocity of visual pattern, as in previous flight simulators driven by torque or ΔWBA^{60,61}. The delay between the fly's movement and the pattern update was less than 20 ms.

The gain factors were set so that the straight flight, verified by visual inspection of real-time video frames, produced straight flight and that a single body saccade⁶², also detected by video inspection, typically rotated the pattern by 30–40°. This value corresponds to the mean body rotation angle elicited by a saccade of flies in a rotatable-tether condition⁶³. The gain factors were adjusted for each animal, and updated during the course of the experiment (see below).

Behavioral experiments. All types of experiments included a 4-s choice period during which a visual pattern was presented in the closed-loop mode. During this period, the fly controlled the rotation of a visual pattern or, equivalently, changed its heading direction in the virtual space. The choice in each trial was defined as the side to which the fly initially rotated by more than 15° (4 pixels). Trials in which the fly did not make a choice (that is, the maximum cumulative pattern rotation of 15° or less) were discarded from further analyses. Trials were also discarded when the fly made a choice earlier than 50 ms from the onset of targets, which corresponds to the time of tethered flies to change yaw torque in response to bar displacement⁶⁴. When the fly stopped flying, a puff of air was applied to initiate flight. We terminated the experiment and discarded the data when the same fly stopped flying for the third time during the experiment. The definition of choices, the criteria for trial disposal, and the termination rule were pre-established and maintained throughout all the experiments. Trials of different stimulus conditions were randomly interleaved with an inter-trial-interval of 3–5 s. Each fly completed (that is, made a choice without meeting the criteria for disposal) ten trials for each stimulus condition unless otherwise noted.

In the cueing experiment, each trial began by a 2-s open-loop period during which a cue stimulus was presented either in the left or the right visual field with the horizontal eccentricity of 60° (which we denote –60° and +60°, respectively). This was followed by a 1-s delay period of uniform illumination, and then the choice period with simultaneous presentation of two target stimuli, one in each visual field, with the eccentricity of 60° (±60°). In the bar choice experiment, a single bar (+60° or –60°) or two bars (±60°) were presented in the closed-loop mode for 4 s. Trials of the cueing experiment and the bar choice experiment were randomly interleaved in the same session. Each fly completed 20 trials for each stimulus condition.

In the following experiments, the task was identical to the cueing experiment with some modifications. In the cue/target location experiment, the cue appeared

in one of the ten locations, chosen randomly across trials, and the target location varied across flies (either $\pm 45^\circ$, $\pm 60^\circ$ or $\pm 75^\circ$). In the cue duration and delay duration experiments, the duration of the cue and the delay period varied across trials, respectively. In the closed-loop cue experiment, the cue was presented for 1 s in closed-loop with the initial position either at $+60^\circ$ or -60° . In the cueing experiment with bright bars, bright bars were used as cue and target stimuli.

The cueing and single bar experiment contained three conditions. In 'different' and 'same' conditions, the task was identical to the cueing experiment except that only one bar appeared in the choice period at the opposite or the same location as compared to the cue, respectively. In 'no cue' condition, flies were presented with one bar in the closed-loop mode without any preceding cue. In the bar location experiment, a single bar was presented at one of ten locations in the closed-loop mode for 4 s. In the bar choice experiment with bright bars, the task was identical to the bar choice experiment except that the stimuli were bright bars.

Predictions of the location and the motor hypotheses. The location hypothesis states, by definition, that each curve should peak at the cue location that matches the target location but provides no further constraints on the shape of the curves. To illustrate the prediction of the hypothesis, we made the curve shape to be Gaussian of the s.d. of 15° . Note that this width of the curve was used only for generating schematic curves but not in the evaluation of the hypothesis. The schematic curves of the motor hypothesis were generated by performing polynomial interpolation on the mean percentage of bar choice data in **Supplementary Figure 1u**.

Behavioral genetics experiments. Six Gal4 driver lines labeling subsets of ring neurons (**Supplementary Fig. 14**) were crossed with flies carrying *UAS-Kir2.1^{AAE}-GFP*. These crosses resulted in viable adult flies in three of the six Gal4 lines (*R38H02-Gal4*, *R15B07-Gal4*, and *c232-Gal4*). As a control, the three Gal4 lines and *UAS-Kir2.1^{AAE}-GFP* flies were also crossed with the wild-type flies. Each of these flies performed the cueing task and the bar choice task as in the behavioral experiment (see above), except that each fly performed 19 or 20 trials for each condition.

Calcium imaging. Two-photon calcium imaging was conducted as described previously⁶⁵ with a few modifications. A 40 \times objective lens (Objective W Plan-Apochromat 40 \times /1.0 DIC, Zeiss) was used. We identified the BU in the right hemisphere using the baseline fluorescence of GCaMP6f. In each fly, we manually targeted one of the ten target planes that equally divide the BU along the dorsal-ventral axis (**Fig. 3f** and **Supplementary Fig. 3c**). Images were acquired from a single plane at 19.7 frames per s (160 \times 160 pixels, pixel size = 0.19 μ m, dwell time = 1.6 μ s) with 930-nm light (laser power measured at the back aperture was below 20 mW). At the end of most experiments, we obtained a stack of high-resolution images (320 \times 320 pixels, pixel size = 0.095 μ m) that covered the BU at 0.5 μ m step (**Supplementary Fig. 3b**).

During calcium imaging, flies performed the same task as in the cueing experiment except that the duration of the delay period was extended to 4 s. We made the delay period substantially longer than the decay kinetics of GCaMP6f (half-life of <0.5 s)^{56,66}, so that neural activity during the delay period can be reliably distinguished from activity during the cue period. The recording lasted until the fly stopped flying for the third time during the experiment. We analyzed the data only if the fly completed at least ten trials for each cue location (13.6 ± 4.2 trials, mean \pm s.d. for each cue location, $N = 40$ flies). The inter-trial-interval was 9 s.

The choice bias during calcium imaging (the percentage of uncued choice, $55.4 \pm 1.2\%$, mean \pm s.e.m., $N = 40$ flies) was weaker than that observed for the same delay duration in behavioral experiments ($61.5 \pm 2.6\%$, mean \pm s.e.m., $N = 20$ flies; **Supplementary Fig. 1i**). This is to be expected because a larger fraction of the fly's body was glued to the holding plate, the fly had undergone dissection, and parts of the legs were removed in calcium imaging experiments. Differences in genotypes might have contributed as well.

Experimental protocol. After being placed in the experimental setup, the fly underwent an approximately 3 min of adaptation period under the background illumination. Air puff was applied to initiate flight if the fly was not flying at the end of the adaptation period. The fly then navigated in a closed-loop mode with a single bar for 2–5 min during which the gain factors were set. The fly was tested further only when it kept flying and showed any response to the bar during this

calibration period in behavioral and calcium imaging experiments. This criterion was not used in behavioral genetics experiments because the inactivation of ring neurons might impair responses to the bar. The gain factors were adjusted typically once every two minutes during the course of the experiment to maintain the relationship between body saccades and pattern rotation. Note that this calibration was done at the point where the fly completed an equal number of trials for each stimulus condition, ensuring that the calibration would not produce any condition-specific choice bias. During behavioral experiments, a weak stream of air was continuously applied to the fly to keep the humidity constant ($\sim 70\%$ relative humidity, air speed of 0.1 m/s).

Photolabeling using PA-GFP. We characterized the morphology of neurons innervating different parts of the BU using PA-GFP^{67–69}. The brain pan-neuronally expressing PA-GFP was mounted on a glass slide such that the dorsal side was facing upward as in calcium imaging experiments. Under the two-photon microscope, a target volume of the BU in the right hemisphere was identified using the baseline fluorescence of PA-GFP obtained with 930-nm light. To minimize unintended photoactivation, the laser power was kept below 5 mW (measured at the back aperture). The region of interest (ROI), manually defined in a single z section, was photoactivated with 710-nm light (pixel size = 0.12 μ m, dwell time = 2 μ s). Each photoactivation cycle consisted of four consecutive scans of the ROI. After 10–20 cycles of photoactivation, we moved the objective lens to another z section within the target volume and redefined the ROI. Each brain underwent 200 cycles of photoactivation with an inter-cycle-interval of 10 s or longer. Over the course of each experiment, we gradually increased the laser power (from 15 mW up to 40 mW) to achieve reliable photoconversion while avoiding photodamage.

In experiments focusing on the dorsal-ventral axis, target volumes were defined so that each spans one-fifth of the dorsal-ventral extent of the BU. In experiments focusing on the VM and VL parts of the BU, target volumes were defined by dividing the ventral two-fifth of the BU into two along the medial-lateral axis. The VL part corresponds to the region where the contra-preferring microglomeruli primarily reside (**Supplementary Fig. 8c**).

In addition to the EB and the AOTU, photoactivation of the BU labeled a lateral part of the lateral accessory lobe, the contralateral BU, and fibers connecting both parts of the BU running along the anterior-dorsal edge of the fan-shaped body. Because photolabeling of these structures was weak and largely irrespective of the photoactivated volume, we did not analyze it further.

Immunohistochemistry. We performed immunohistochemistry as described previously⁶⁵. As the primary antibodies, we used rat anti-GFP (1:1,000) and mouse nc82 (1:20) in behavioral genetics experiments and for the analysis of BU structure, nc82 (1:20) in PA-GFP experiments, and rat anti-GFP (1:1,000) and rabbit anti-RFP (1:100) for the analysis of ring neuron innervation. As the secondary antibodies, we used anti-rat CF488 (1:250), anti-mouse CF633 (1:250) and anti-rabbit CF633 (1:250). Information about the antibodies is described in the **Life Sciences Reporting Summary**. Images of immunostained brains were acquired using a confocal microscope (FV1000D, Olympus). In **Figure 3b**, we used confocal stacks of the BU (**Supplementary Fig. 3a**) and counted the number of microglomeruli by manually delineating microglomeruli using the Segmentation Editor plugin in Fiji⁷⁰.

Data analysis. Data analyses were performed using MATLAB (MathWorks) unless otherwise noted.

Partial correlation analysis. The predictions of location and motor hypotheses were assessed by performing partial correlation analysis, which quantified the correlation between the choice bias and the prediction of either hypothesis after removing the effect of the other hypothesis. For each combination of cue and target locations, we calculated the choice bias (% uncued choice – 50) averaged across flies (**Fig. 1h**). The location hypothesis predicts that the choice bias depends on the proximity of the cue to the target. Thus, the absolute value of the difference between the cue and the target location ($|\text{cue location} - \text{target location}|$; for example, $15 = |45 - 60|$ for the combination of $\pm 45^\circ$ cue and $\pm 60^\circ$ targets) was used as the variable that determines the choice bias in this hypothesis. The motor hypothesis predicts that the choice bias depends on how much they have turned before the choice (that is, during the cue and the delay periods). Thus,

the mean Δ WBA during either the cue or the delay period (averaged across flies; **Supplementary Fig. 1v**) was used as the predicted determinant of the choice bias in this hypothesis. We used the following formula

$$r_{XY \cdot Z} = \frac{r_{XY} - r_{XY}r_{YZ}}{\sqrt{(1 - r_{XZ}^2)}\sqrt{(1 - r_{YZ}^2)}}$$

where X is the choice bias, Y is the difference between the cue and the target location, Z is the Δ WBA during either the cue or the delay period, and r_{AB} represents the correlation coefficient between A and B .

The choice bias was highly correlated with the difference between the cue and the target location (partial correlation, -0.75 , $P = 0.0018$) but not with the mean Δ WBA during the cue period (partial correlation, 0.39 , $P = 0.17$). The trend was the same when the mean Δ WBA during the delay was used as a variable (partial correlation between the choice bias and the difference between the cue and the target location, -0.82 , $P < 0.001$; between the choice bias and the mean Δ WBA, 0.068 , $P = 0.82$). These results indicate that our data are consistent with the location but not the motor hypothesis.

Analysis of calcium imaging data. To remove motion artifact, imaging data from each animal underwent two steps of image registration, which use an intensity-based algorithm with two-dimensional cross-correlation. At the first step, individual frames in each trial were aligned to the template, which is an average of 40 frames preceding the cue onset (pre-cue period). Then, a baseline image for each trial was calculated as the average of the aligned frames in the pre-cue period. At the second step, frames were aligned across trials based on the baseline images.

To define ROIs corresponding to individual microglomeruli, we used correlation-based k -means clustering because pixels belonging to the same microglomerulus are highly correlated in intensity⁷. After manually delineating the BU using the trial-averaged baseline image, we applied the clustering to time series of pixel values within this area. The number of clusters was set to 25. Although this method properly isolated many microglomeruli, errors occurred at a certain rate (for example, separation of a single microglomerulus, judged by its shape and size, into two clusters). We therefore manually defined ROIs by inspecting an average of frames in which the fluorescence of each cluster was distinct (**Fig. 3e**). After excluding the pixels belonging to more than one ROI, the fluorescence of each ROI (F) was obtained as an average of pixels in each frame. $\Delta F/F$ for each ROI was calculated using the baseline defined by averaging frames immediately before the cue onset (four frames in each trial) within and across trials. In total, we detected 566 ROIs in 40 flies (the number of ROIs per brain, 14.2 ± 2.8 , mean \pm s.d.).

In each microglomerulus, differential activity between ipsilateral and contralateral cue presentations was quantified using receiver operating characteristics (ROC) analysis. The area under the ROC curve (AUC) was calculated based on the average $\Delta F/F$ during the cue period in each trial. The trial-type preference was defined as $2 \cdot (\text{AUC} - 0.5)$, which is the AUC scaled from -1 to 1 (ref. 71). This index represents the performance of an ideal observer that classifies cue location based on the activity of the microglomerulus and its hypothetical counterpart (antineuron) whose activity in the ipsilateral and contralateral cue trials corresponds to the activity of the recorded microglomerulus in the contralateral and ipsilateral cue trials, respectively⁷². The trial-type preference of -1 and 1 indicates the perfect classification with higher activity in ipsilateral and contralateral cue trials, respectively. This index is 0 if the activity is indistinguishable between the two types of trials. To test the statistical significance of the trial-type preference, we performed a permutation test where the trial-type label was randomly shuffled across trials and the trial-type preference was calculated from the shuffled data (2,000 repetitions). The trial-type preference was also calculated based on the activity during the last 3 s of the delay period. This period was chosen by considering the decay kinetics of GCaMP6f (refs. 56,66).

In each microglomerulus, cue location-related and turn-related components of the activity were separated based on linear regression. First, Δ WBA traces were down-sampled to the sampling rate of calcium signals. Second, cross-correlation between $\Delta F/F$ and down-sampled Δ WBA was calculated for each task period. This analysis revealed that only the contra-preferring population showed prominent turn-related activity consistently across task periods (**Supplementary Fig. 5a–c**). Therefore, we calculated cross-correlation for this population using the entire task period and obtained the time lag that maximized the correlation (**Supplementary**

Fig. 5d,e). Δ WBA traces were then shifted by the median of this lag (five time frames, 255 ms) for the following analyses. For each cue location, linear regression was performed at each task period (**Fig. 4a,b** and **Supplementary Fig. 5f**) or each time frame (**Fig. 4c–j** and **Supplementary Fig. 6**) as follows

$$\Delta F/F = S \cdot \Delta \text{WBA} + Y$$

where S is the slope of the regression line and Y is the Y -intercept. These parameters were determined using the linear least-squares method. The slope represents the linear dependency of $\Delta F/F$ on Δ WBA, with a positive sign corresponding to higher calcium responses for intended turns toward the contralateral side. The Y -intercept represents the component of activity that is not explained by Δ WBA. Thus, the Y -intercept represents the baseline activity during the 'pre' period, responses to cue during the cue and the delay periods, and responses to choice targets and cue during the choice period. The slope represents the selectivity for turns during the pre, the cue and the delay periods. It also represents the motion of choice targets during the choice period. We quantified the selectivity for cue location by averaging Y -intercept differences across time frames (**Fig. 4h** and **Supplementary Fig. 6j,k**). To quantify the selectivity for turns, the slopes for the entire task period were averaged across time frames and cue locations (**Fig. 4j** and **Supplementary Fig. 6k**). In **Fig. 4a,b**, Δ WBA of individual time frames was grouped using equally sized bins (size, 5°) for visibility. The same binning was also used to evaluate the quality of the regression fit (**Supplementary Fig. 5f**). The regression line was obtained separately for each task period, and the coefficient of determination (R^2) was calculated between the prediction from the regression lines and mean $\Delta F/F$ at each bin (for example, **Fig. 4a,b**).

A relationship between the activity of a microglomerulus and the angle of each wing was assessed after removing the cue location component (**Supplementary Fig. 7a–c**). First, we performed the same regression analysis as in **Fig. 4** except that the time-shifted angle of each wing was used as an independent variable. Then, we subtracted the Y -intercept of the fitted line from $\Delta F/F$ at every time frame. Finally, we calculated the turn score as Pearson's correlation coefficient between the time-shifted WBA and the Y -intercept-compensated $\Delta F/F$. Positive turn scores correspond to higher activity for contralateral turns (that is, larger and smaller WBAs for ipsilateral and contralateral wings, respectively). The same method was used to calculate turn scores for Δ WBA. For separating turns of different temporal characteristics (**Supplementary Fig. 7d–g**), raw Δ WBA traces were low-pass filtered at 1-Hz to define a low-frequency component of turns. We subtracted the low-frequency component from the raw trace to obtain a high-frequency component of turns. Note that in a previous study⁴⁴, a similar filtering was used to extract the component corresponding to body saccades. Turn scores for these components were calculated as for Δ WBA.

To detect calcium transients, we first filtered the $\Delta F/F$ trace in individual trials with a boxcar filter of five frames (255 ms) (**Supplementary Fig. 10b,c**). We then calculated the derivative of the filtered trace, followed by another filtering with the same boxcar filter (**Supplementary Fig. 10c**). We defined the onset of a transient as the time at which the filtered derivative function became larger than a threshold ($1 \Delta F/F/s$). The inter-transient interval was defined as the interval between the onsets of two successive transients (**Supplementary Fig. 10j,p**). To characterize the dynamics of individual transients, we analyzed the trials in which only one transient occurred in the last 3 s of the delay period with its onset in the first 1 s of this 3-s period (**Supplementary Fig. 10f,g,k–m,q–s**). The peak of the transient was defined as the time frame at which the filtered $\Delta F/F$ trace reached the maximum value within 40 frames (2.03 s) from the transient onset. The peak amplitude was defined as the difference in the filtered $\Delta F/F$ value between the transient onset and the peak. The duration of the transient was defined as the interval between the transient onset and the time filtered $\Delta F/F$ decreased to half the peak amplitude. We also detected the transients using the threshold which was half the original value ($0.5 \Delta F/F/s$) in **Supplementary Figure 11d,h** to examine the effect of our choice of threshold.

Analysis of PA-GFP data. To compare photolabeling across brains, confocal stacks were aligned to a standard brain (JFRC2)⁷³ based on nc82 images. Image registration was carried out by performing affine transformation to maximize the correlation in the intensity fluctuations. We performed the registration separately for each brain region using rectangular solids as the registration targets. For the analysis of the AOTU, the registration target just enclosed the AOTU. For the analysis of the EB and the BU, the registration target enclosed the EB and the BU

and contained parts of the mushroom body and the fan-shaped body. Binary images showing the brain regions were generated based on the standard brain and its associated labels of brain structures.

We used the ImageJ's Smooth function (3×3 pixels mean filter) to generate the images shown in **Figures 2b** and **6c** and **Supplementary Figures 2a** and **12b**. We reduced the brightness and contrast of nc82 channel for the images in **Figure 6c** for better visibility of PA-GFP signals.

Statistics. We predetermined sample sizes not using any statistical methods but based on effect sizes and sample-by-sample variability observed in pilot experiments. We chose parametric statistical tests based on inspection of the data distribution without employing formal tests. The variance of data was not statistically compared except for **Supplementary Figure 2b**. All statistical tests were two-sided. Corrections for multiple comparisons were performed where appropriate. Neither randomization nor blinding was performed for the group allocation during experiments or data analysis. Exact *P* values for all statistical tests can be found in **Supplementary Table 1**.

A Life Sciences Reporting Summary is available.

Data and code availability. Data and code used in this study are available upon reasonable request.

50. Vanin, S. *et al.* Unexpected features of *Drosophila* circadian behavioral rhythms under natural conditions. *Nature* **484**, 371–375 (2012).
51. Bhandawat, V., Maimon, G., Dickinson, M.H. & Wilson, R.I. Olfactory modulation of flight in *Drosophila* is sensitive, selective and rapid. *J. Exp. Biol.* **213**, 3625–3635 (2010).
52. Pfeiffer, B.D., Truman, J.W. & Rubin, G.M. Using translational enhancers to increase transgene expression in *Drosophila*. *Proc. Natl. Acad. Sci. USA* **109**, 6626–6631 (2012).
53. Paradis, S., Sweeney, S.T. & Davis, G.W. Homeostatic control of presynaptic release is triggered by postsynaptic membrane depolarization. *Neuron* **30**, 737–749 (2001).
54. Pfeiffer, B.D. *et al.* Tools for neuroanatomy and neurogenetics in *Drosophila*. *Proc. Natl. Acad. Sci. USA* **105**, 9715–9720 (2008).
55. Pfeiffer, B.D. *et al.* Refinement of tools for targeted gene expression in *Drosophila*. *Genetics* **186**, 735–755 (2010).
56. Chen, T.W. *et al.* Ultrasensitive fluorescent proteins for imaging neuronal activity. *Nature* **499**, 295–300 (2013).
57. Yang, M.Y., Armstrong, J.D., Vilinsky, I., Strausfeld, N.J. & Kaiser, K. Subdivision of the *Drosophila* mushroom bodies by enhancer-trap expression patterns. *Neuron* **15**, 45–54 (1995).
58. Straw, A.D. & Dickinson, M.H. Motmot, an open-source toolkit for real-time video acquisition and analysis. *Source Code Biol. Med.* **4**, 5 (2009).
59. Reiser, M.B. & Dickinson, M.H. A modular display system for insect behavioral neuroscience. *J. Neurosci. Methods* **167**, 127–139 (2008).
60. Heisenberg, M. & Wolf, R. *Vision in Drosophila: Genetics of Microbehavior* (Springer-Verlag, 1984).
61. Maimon, G., Straw, A.D. & Dickinson, M.H. A simple vision-based algorithm for decision making in flying *Drosophila*. *Curr. Biol.* **18**, 464–470 (2008).
62. Tammero, L.F. & Dickinson, M.H. The influence of visual landscape on the free flight behavior of the fruit fly *Drosophila melanogaster*. *J. Exp. Biol.* **205**, 327–343 (2002).
63. Bender, J.A. & Dickinson, M.H. Visual stimulation of saccades in magnetically tethered *Drosophila*. *J. Exp. Biol.* **209**, 3170–3182 (2006).
64. Heisenberg, M. & Wolf, R. Reafferent control of optomotor yaw torque in *Drosophila melanogaster*. *J. Comp. Physiol. A Neuroethol. Sens. Neural Behav. Physiol.* **163**, 373–388 (1988).
65. Badel, L., Ohta, K., Tsuchimoto, Y. & Kazama, H. Decoding of context-dependent olfactory behavior in *Drosophila*. *Neuron* **91**, 155–167 (2016).
66. Schnell, B., Weir, P.T., Roth, E., Fairhall, A.L. & Dickinson, M.H. Cellular mechanisms for integral feedback in visually guided behavior. *Proc. Natl. Acad. Sci. USA* **111**, 5700–5705 (2014).
67. Datta, S.R. *et al.* The *Drosophila* pheromone cVA activates a sexually dimorphic neural circuit. *Nature* **452**, 473–477 (2008).
68. Patterson, G.H. & Lippincott-Schwartz, J. A photoactivatable GFP for selective photolabeling of proteins and cells. *Science* **297**, 1873–1877 (2002).
69. Ruta, V. *et al.* A dimorphic pheromone circuit in *Drosophila* from sensory input to descending output. *Nature* **468**, 686–690 (2010).
70. Schindelin, J. *et al.* Fiji: an open-source platform for biological-image analysis. *Nat. Methods* **9**, 676–682 (2012).
71. Feierstein, C.E., Quirk, M.C., Uchida, N., Sosulski, D.L. & Mainen, Z.F. Representation of spatial goals in rat orbitofrontal cortex. *Neuron* **51**, 495–507 (2006).
72. Britten, K.H., Shadlen, M.N., Newsome, W.T. & Movshon, J.A. The analysis of visual motion: a comparison of neuronal and psychophysical performance. *J. Neurosci.* **12**, 4745–4765 (1992).
73. Jenett, A. *et al.* A GAL4-driver line resource for *Drosophila* neurobiology. *Cell Rep.* **2**, 991–1001 (2012).

Life Sciences Reporting Summary

Nature Research wishes to improve the reproducibility of the work that we publish. This form is intended for publication with all accepted life science papers and provides structure for consistency and transparency in reporting. Every life science submission will use this form; some list items might not apply to an individual manuscript, but all fields must be completed for clarity.

For further information on the points included in this form, see [Reporting Life Sciences Research](#). For further information on Nature Research policies, including our [data availability policy](#), see [Authors & Referees](#) and the [Editorial Policy Checklist](#).

► Experimental design

1. Sample size

Describe how sample size was determined.

We predetermined sample sizes not using any statistical methods but based on effect sizes and sample-by-sample variability observed in pilot experiments.

2. Data exclusions

Describe any data exclusions.

We excluded the data when animals failed to complete a predetermined number of trials in behavioral, behavioral genetics, and calcium imaging experiments. Criteria were established prior to data collection as described in "Behavioral experiments" and "Calcium imaging" in Methods.

3. Replication

Describe whether the experimental findings were reliably reproduced.

The experimental findings were reliably reproduced as shown in the figures where we showed the entire distribution of data where appropriate. We showed only example data for the results of immunostaining experiments because the high repeatability of the method (Gal4-UAS based fluorescent protein expression) has been widely recognized in the field.

4. Randomization

Describe how samples/organisms/participants were allocated into experimental groups.

No randomization was used in sample allocation. Rather, we controlled the effects of covariates by systematically allocate samples into groups (e.g., sample #1 for group 1, sample #2 for group 2, sample #3 for group 1, sample #4 for group 2, and so on).

5. Blinding

Describe whether the investigators were blinded to group allocation during data collection and/or analysis.

Blinding was not relevant in all but behavioral genetics experiments where no blinding was used because of the limitation of human resource.

Note: all studies involving animals and/or human research participants must disclose whether blinding and randomization were used.

6. Statistical parameters

For all figures and tables that use statistical methods, confirm that the following items are present in relevant figure legends (or in the Methods section if additional space is needed).

n/a Confirmed

- ☐ ☒ The exact sample size (n) for each experimental group/condition, given as a discrete number and unit of measurement (animals, litters, cultures, etc.)
- ☐ ☒ A description of how samples were collected, noting whether measurements were taken from distinct samples or whether the same sample was measured repeatedly
- ☐ ☒ A statement indicating how many times each experiment was replicated
- ☐ ☒ The statistical test(s) used and whether they are one- or two-sided (note: only common tests should be described solely by name; more complex techniques should be described in the Methods section)
- ☐ ☒ A description of any assumptions or corrections, such as an adjustment for multiple comparisons
- ☐ ☒ The test results (e.g. P values) given as exact values whenever possible and with confidence intervals noted
- ☐ ☒ A clear description of statistics including central tendency (e.g. median, mean) and variation (e.g. standard deviation, interquartile range)
- ☐ ☒ Clearly defined error bars

See the web collection on [statistics for biologists](#) for further resources and guidance.

► Software

Policy information about [availability of computer code](#)

7. Software

Describe the software used to analyze the data in this study.

Data were analyzed using custom code written in MATLAB (MathWorks, 2012a, 2013a, 2015b).

For manuscripts utilizing custom algorithms or software that are central to the paper but not yet described in the published literature, software must be made available to editors and reviewers upon request. We strongly encourage code deposition in a community repository (e.g. GitHub). *Nature Methods* [guidance for providing algorithms and software for publication](#) provides further information on this topic.

► Materials and reagents

Policy information about [availability of materials](#)

8. Materials availability

Indicate whether there are restrictions on availability of unique materials or if these materials are only available for distribution by a for-profit company.

N/A

9. Antibodies

Describe the antibodies used and how they were validated for use in the system under study (i.e. assay and species).

rat anti-GFP (nacalai tesque Cat# 04404-84, RRID:AB_10013361), mouse nc82 (DSHB Cat# nc82, RRID:AB_528108), rabbit anti-RFP (Abcam Cat# ab62341, RRID:AB_945213), Goat Anti-Rat CF488A (Biotium inc Cat#20023, RRID:AB_10557403), Goat Anti-Mouse CF633 (Biotium inc Cat#20120, RRID:AB_10556971), Goat Anti-Rabbit CF633 (Biotium inc Cat#20122, RRID:AB_10559042). All antibodies are widely used in the field.

10. Eukaryotic cell lines

a. State the source of each eukaryotic cell line used.

N/A

b. Describe the method of cell line authentication used.

N/A

c. Report whether the cell lines were tested for mycoplasma contamination.

N/A

d. If any of the cell lines used are listed in the database of commonly misidentified cell lines maintained by [ICLAC](#), provide a scientific rationale for their use.

N/A

► Animals and human research participants

Policy information about [studies involving animals](#); when reporting animal research, follow the [ARRIVE guidelines](#)

11. Description of research animals

Provide details on animals and/or animal-derived materials used in the study.

Drosophila melanogaster, females, 2 to 3 days after eclosion.

Policy information about [studies involving human research participants](#)

12. Description of human research participants

Describe the covariate-relevant population characteristics of the human research participants.

N/A